# Noninvasive brain cancer imaging with a bispecific antibody fragment, generated via click chemistry

Haiming Luo[a,1], Reinier Hernandez[b,1], Hao Hong[a], Stephen A. Graves[b], Yunan Yang[a], Christopher G. England[b], Charles P. Theuer[c], Robert J. Nickles[b], and Weibo Cai[a,b,d,e,2]

[a]Department of Radiology, University of Wisconsin–Madison, Madison, WI 53705; [b]Department of Medical Physics, University of Wisconsin–Madison, Madison, WI 53705; [c]TRACON Pharmaceuticals, Inc., San Diego, CA 92122; [d]Materials Science Program, University of Wisconsin–Madison, Madison, WI 53705; and [e]University of Wisconsin Carbone Cancer Center, Madison, WI 53705

Edited by Michael E. Phelps, University of California, Los Angeles, CA, and approved August 27, 2015 (received for review May 17, 2015)

**Early diagnosis remains a task of upmost importance for reducing cancer morbidity and mortality. Successful development of highly specific companion diagnostics targeting aberrant molecular pathways of cancer is needed for sensitive detection, accurate diagnosis, and opportune therapeutic intervention. Herein, we generated a bispecific immunoconjugate [denoted as Bs-F(ab)$_2$] by linking two antibody Fab fragments, an anti-epidermal growth factor receptor (EGFR) Fab and an anti-CD105 Fab, via bioorthogonal "click" ligation of *trans*-cyclooctene and tetrazine. PET imaging of mice bearing U87MG (EGFR/CD105$^{+/+}$) tumors with $^{64}$Cu-labeled Bs-F(ab)$_2$ revealed a significantly enhanced tumor uptake [42.9 ± 9.5 percentage injected dose per gram (%ID/g); $n = 4$] and tumor-to-background ratio (tumor/muscle ratio of 120.2 ± 44.4 at 36 h postinjection; $n = 4$) compared with each monospecific Fab tracer. Thus, we demonstrated that dual targeting of EGFR and CD105 provides a synergistic improvement on both affinity and specificity of $^{64}$Cu-NOTA-Bs-F(ab)$_2$. $^{64}$Cu-NOTA-Bs-F(ab)$_2$ was able to visualize small U87MG tumor nodules (<5 mm in diameter), owing to high tumor uptake (31.4 ± 10.8%ID/g at 36 h postinjection) and a tumor/muscle ratio of 76.4 ± 52.3, which provided excellent sensitivity for early detection. Finally, we successfully confirmed the feasibility of a ZW800-1–labeled Bs-F(ab)$_2$ for near-infrared fluorescence imaging and image-guided surgical resection of U87MG tumors. More importantly, our rationale can be used in the construction of other disease-targeting bispecific antibody fragments for early detection and diagnosis of small malignant lesions.**

glioblastoma | bispecific antibody fragment | EGFR | CD105 | positron emission tomography (PET)

Despite advances in diagnostic procedures and clinical patient management, early detection and diagnosis of cancers remains the most important endeavor for reducing cancer morbidity and mortality (1). Although ultrasonography, computed tomography (CT), and magnetic resonance imaging are essential to clinical oncology, tumor detection using these technologies is based primarily on anatomical characteristics, providing limited information about the molecular profile during tumor progression (2). On the other hand, noninvasive molecular imaging techniques, which can be designed to specifically detect alterations in gene amplification or mutations that occur early during cancer progression, have the potential to visualize carcinogenesis at earlier stages (3). Given its excellent sensitivity (picomolar range), adequate spatial resolution, and the ability to accurately quantify the biodistribution of a radiotracer, PET imaging is becoming the modality of choice to noninvasively study the biochemistry of human tumors in situ (4). PET imaging with $^{18}$F-fluorodeoxyglucose ($^{18}$F-FDG), which allows clinicians to scrutinize glucose metabolism in vivo, has largely dominated the clinical diagnostic oncology setting. However, a common disadvantage of the use of $^{18}$F-FDG as an imaging tracer has been its limited sensitivity and specificity, which can lead to confounding diagnosis (5); other pathological processes including inflammation and infection also present high glucose metabolism. Additionally, $^{18}$F-FDG PET often fails at detecting small malignant lesions (<5 mm in diameter) (6). Therefore, there is a pressing need for the implementation of molecular imaging probes that specifically target cancer-associated biological pathways and that can detect earlier such processes at the molecular level (7).

Antibodies are of high interest as molecular imaging agents, particularly in oncology, because of their excellent antigen specificity and binding affinity. ImmunoPET probes can be designed to seek and target tumor cell-specific surface epitopes in vivo while maintaining low off-target effects (8). This enables the acquisition of high-quality PET images, which is highly desirable for cancer diagnosis, staging, and therapy response assessment. Compared with $^{18}$F-FDG and several other small-molecule PET tracers, antibodies provide greater specificity and phenotypic information on primary and metastatic diseases that can guide treatment decisions (3). However, the implementation of antibody-based imaging has been limited by practical complications related to long circulation half-lives, slow tumor penetration, immunogenicity, and regulatory hurdles. Fortunately, various protein engineering technologies can alleviate many of these issues. For example, humanized and fully human antibodies are available that minimized the risk of eliciting host immune responses. Furthermore, antibody fragments can exhibit significantly improved pharmacokinetic profiles compared with the intact antibody while retaining excellent antigen-binding affinity. A myriad of such immunoderivatives have been used for immunoPET imaging including monovalent fragments, diabodies, triabodies, minibodies, and single-domain antibodies (9). However, although PET imaging with antibody fragments offers several advantages in terms of radiation exposure, time to image, and multiple/repeated imaging, the fragments typically display

## Significance

Given the success of combination therapies for the treatment of cancer, the use of bispecific antibodies targeting multiple cancerous molecular pathways is an attractive strategy to enhance the efficacy of current therapeutic paradigms. However, parallel development of companion diagnostic tools is essential for patient identification, stratification, and the early assessment of treatment efficacies. Herein, we describe the generation of a bispecific construct for noninvasive PET imaging of glioblastoma via bioorthogonal click chemistry. The excellent tumor-homing properties displayed by our bispecific probe, which features two antibody fragments simultaneously targeting epidermal growth factor receptor and CD105, demonstrated that our approach is a simple and effective method to generate multispecific targeting agents for noninvasive molecular imaging.

Author contributions: H.L., R.H., H.H., and W.C. designed research; H.L., R.H., S.A.G., Y.Y., and C.G.E. performed research; C.P.T. and R.J.N. contributed new reagents/analytic tools; H.L. and R.H. analyzed data; and H.L., R.H., and W.C. wrote the paper.

The authors declare no conflict of interest.

This article is a PNAS Direct Submission.

[1]H.L. and R.H. contributed equally to this work.

[2]To whom correspondence should be addressed. Email: wcai@uwhealth.org.

This article contains supporting information online at www.pnas.org/lookup/suppl/doi:10.1073/pnas.1509667112/-/DCSupplemental.



www.pnas.org/cgi/doi/10.1073/pnas.1509667112

significantly reduced tumor uptake and a much higher renal accumulation (10, 11).

Given the inherent complexity of cancer, which involves a sophisticated cross-talk and promiscuity between multiple disease-mediating pathways and growth-promoting factors, targeting an isolated process usually fails to provide a satisfactory diagnosis and treatment efficacy (12). On the other hand, bispecific antibody fragments simultaneously targeting two antigens make for a promising alternative to enhance tumor uptake as well as specificity (13, 14). Although the value of bispecific antibodies for combination therapies has been proposed (15, 16), their potential as molecular imaging agents for cancer detection remains largely unexplored.

Herein, we developed a bispecific construct, Bs-F(ab)$_2$—via conjugation of two antibody Fab fragments targeting epidermal growth factor receptor (EGFR) and CD105, respectively—for radiolabeling with $^{64}$Cu and noninvasive PET imaging. The antibody fragments were obtained by enzymatic digestion of cetuximab (CET), an anti-human EGFR chimeric mAb, and TRC105, a mAb that recognizes both human and murine CD105. To conjugate the two Fab fragments, we exploited the fast reaction kinetics and selectivity of the inverse electron-demand Diels–Alder reaction between electron-deficient tetrazine (Tz) and strained transcyclooctene (TCO) derivatives (17). EGFR has been extensively studied as a target for anticancer therapy, and its activation stimulates tumor proliferation and angiogenesis (18). Similarly, CD105 (also called endoglin) is abundantly expressed on activated endothelial cells, and such overexpression is a negative prognostic factor in many malignant tumor types (19, 20). To date, simultaneous targeting of EGFR and CD105 has not been investigated. We hypothesized that our bispecific Bs-F(ab)$_2$ will harness the targeting capabilities of CET-Fab and TRC105-Fab and display a synergistic effect via dual targeting of EGFR and CD105. To test our hypothesis, we determined the advantages of dual EGFR/CD105 targeting in terms of tumor-binding affinity and specificity of Bs-F(ab)$_2$ in a glioblastoma multiforme (GBM) xenograft model, which expresses high levels of both EGFR and CD105 ($^{+/+}$). We presented here a generalizable rationale that could be potentially applied to produce bispecific imaging probes from other disease-targeting antibody fragments.

## Results

**Synthesis and Characterization of Bs-F(ab)$_2$.** Monovalent antibody fragments (Fab) were produced from intact CET and TRC105 mAb via papain digestion and purified by size exclusion chromatography and protein A affinity column. The purity of the obtained fragments was confirmed by SDS polyacrylamide gel electrophoresis (SDS/PAGE) and size exclusion chromatography (Fig. 1*B* and Fig. S1). To prepare each Fab fragment for the subsequent conjugation, we derivatized Fab reactive primary amines with one of two reactive moieties of the Diels–Alder orthogonal reactive pair: Tz or TCO. Conjugates were then purified by size exclusion spin columns and concentrated by ultrafiltration. Following, the fragments were covalently linked via a copper-free click reaction to form a bispecific Bs-F(ab)$_2$ antibody fragment (Fig. 1*A*). Size exclusion chromatography showed a reaction efficiency of 37.5% (Fig. S1). SDS/PAGE (Fig. 1*B*) and MALDI-TOF mass spectrometry (Fig. S2) corroborated the identity of Bs-F(ab)$_2$ ([M+H]$^+$, 104.04 kDa).

**In Vitro Studies of Bs-F(ab)$_2$.** To test the binding affinity and bispecificity of Bs-F(ab)$_2$, we carried out flow cytometry and fluorescence microscopy experiments in U87MG cells, which express high levels of both CD105 and EGFR (21, 22). Compared with CET-Fab and TRC105-Fab, Bs-F(ab)$_2$ revealed a significantly stronger immunofluorescence staining of U87MG cells (Fig. 1*C*), which was effectively blocked when cells were incubated with a saturating dose of CET or TRC105, before cell staining. In agreement with fluorescent microscopy, flow cytometry data revealed marked enhancement in fluorescence signal when U87MG cells were incubated with Bs-F(ab)$_2$ instead of each monovalent Fab fragment (Fig. S3). Similarly, CD105 and EGFR blocking was proven effective by flow cytometry studies. There results demonstrated that dual targeting of CD105 and EGFR resulted in enhanced binding affinity and specificity of Bs-F(ab)$_2$ for U87MG cells.

Finally, a competitive binding assay was performed to quantify and compare the binding affinities of Bs-F(ab)$_2$, CET-Fab, and TRC105-Fab to U87MG cells (Fig. 1*D*). The results of the binding isotherm showed a concentration-dependent displacement of bound $^{64}$Cu-NOTA-Bs-F(ab)$_2$ with IC$_{50}$ values of 4.53 ± 0.77, 393 ± 84, and 850 ± 720 nM for Bs-F(ab)$_2$, CET-Fab, and

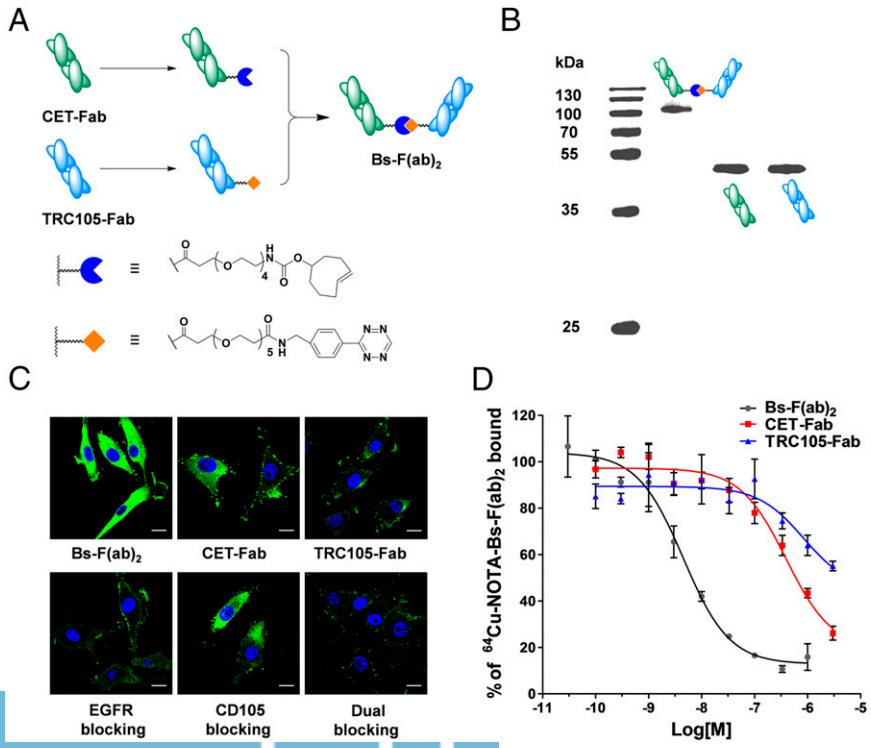


**Fig. 1.** Synthesis and in vitro characterization of Bs-F(ab)$_2$. (*A*) Schematic representation of the synthesis of Bs-F(ab)$_2$. (*B*) SDS/PAGE gel confirming the identity and purity of Bs-F(ab)$_2$. (*C*) Confocal images of U87MG cells incubated with FITC-labeled Bs-F(ab)$_2$, CET-Fab, TRC105-Fab, or Bs-F(ab)$_2$ coincubated with an excess of either CET, TRC105, or both antibodies. (Scale bar, 20 μm.) (*D*) Competitive binding assay comparing the binding affinities of Bs-F(ab)$_2$ (circles), CET-Fab (squares), and TRC105-Fab (triangles). IC$_{50}$ values were markedly lower for Bs-F(ab)$_2$ (4.53 ± 0.77 nM) compared with CET-Fab (393 ± 84 nM) and TRC105-Fab (850 ± 720 nM).

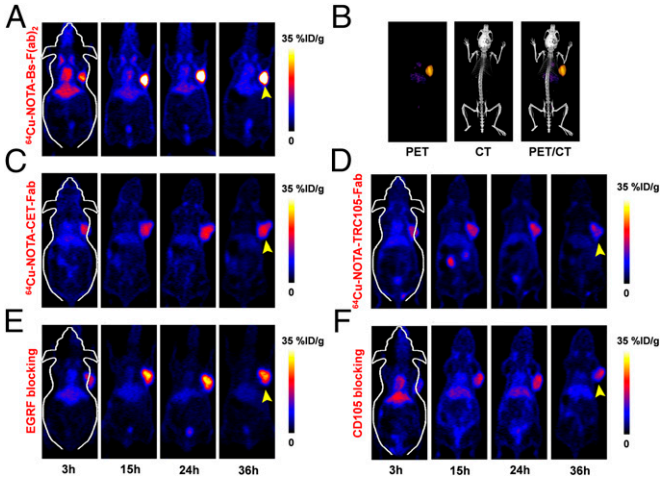


**Fig. 2.** In vivo PET imaging of dual EGFR and CD105 expression with Bs-F(ab)$_2$ tracer in U87MG tumor-bearing mice. Serial coronal PET images of $^{64}$Cu-NOTA-Bs-F(ab)$_2$ (*A*), its PET/CT rendering at 36 h p.i. (*B*), $^{64}$Cu-NOTA-CET-Fab (*C*), and $^{64}$Cu-NOTA-TRC105-Fab (*D*) at 3, 15, 24, and 36 h p.i. of each tracer. Both EGFR (*E*) and CD105 (*F*) blocking resulted in a significant decrease in U87MG tumor uptake of $^{64}$Cu-NOTA-Bs-F(ab)$_2$ ($n$ = 4).

TRC105-Fab, respectively. Only a partial displacement of the bound radioligand was observed at high concentrations (μM) of the competing antibody fragments, demonstrating the ambivalent nature of Bs-F(ab)$_2$ binding.

**Bs-F(ab)$_2$ Shows Enhanced Tumor-Specific Targeting in Vivo.** We used noninvasive PET imaging to determine and compare the tumor-homing properties of Bs-F(ab)$_2$, CET-Fab, and TRC105-Fab. Each antibody fragment was conjugated with the chelator 1,4,7-triazacyclononane-1,4,7-triacetic acid (NOTA) and radiolabeled with $^{64}$Cu with excellent yields (80–90%) and radiochemical purity (>95%). Athymic nude mice bearing U87MG (CD105/EGFR $^{+/+}$) tumors were intravenously (i.v.) administered 150–300 μCi of $^{64}$Cu-NOTA-Bs-F(ab)$_2$, $^{64}$Cu-NOTA-CET-Fab, or $^{64}$Cu-NOTA-TRC105-Fab, and serial static PET scans were acquired at 3, 15, 24, and 36 h postinjection (p.i.). These time points were chosen based on our previous experience on PET imaging using mono and divalent antibody fragments (23, 24). PET images of coronal slices containing U87MG tumors showed fast and elevated tumor accretion of all three tracers that allowed clear delineation of tumor xenografts. However, $^{64}$Cu-NOTA-Bs-F(ab)$_2$ displayed significantly higher ($P$ < 0.001) tumor accumulation than that of the two monovalent fragments (Fig. 2*A*). Coregistered PET/CT images of U87MG-bearing mice reiterated the high tumor contrast and provided anatomical information (Fig. 2*B*).

Region of interest (ROI) analysis of PET images was performed to quantify the tracer uptake as percentage injected dose per gram (%ID/g) in U87MG tumors as well as in off-target tissues including blood pool, liver, kidneys, and muscle. As clearly indicated in the PET images (Figs. 2*A* and 3*A*), $^{64}$Cu-NOTA-Bs-F(ab)$_2$ displayed early high tumor accretion (32.1 ± 6.9%ID/g at 3 h p.i.), which peaked at 47.5 ± 6.7%ID/g ($n$ = 4) at 15 h p.i. Maximum tumor uptake of $^{64}$Cu-NOTA-CET-Fab and $^{64}$Cu-NOTA-TRC105-Fab was significantly lower ($P$ < 0.01), with values of 14.4 ± 1.1%ID/g and 14.3 ± 6.6%ID/g ($n$ = 4), respectively (Fig. 2 *C* and *D* and Fig. 3 *B* and *C*). Consistent with its higher molecular weight, $^{64}$Cu-NOTA-Bs-F(ab)$_2$ showed a longer blood circulation and primarily hepatic clearance that was evidenced by the liver uptake (21.4 ± 3.2–8.4 ± 0.9%ID/g) and blood radioactivity (12.7 ± 3.7–4.9 ± 4.2%ID/g), which gradually decreased from 3 to 36 h p.i. ($n$ = 4; Fig. 3*A*). Liver uptake of $^{64}$Cu-NOTA-CET-Fab and $^{64}$Cu-NOTA-TRC105-Fab was lower, indicating less dominant hepatic clearance of the Fab fragments (Fig. 3 *B* and *C* and Table S1). Kidney uptake was comparable between $^{64}$Cu-NOTA-Bs-F(ab)$_2$ and $^{64}$Cu-NOTA-CET-Fab. However, significantly higher uptake was observed for $^{64}$Cu-NOTA-TRC105-Fab, demonstrating renal clearance as the major excretion pathway for this tracer. All three tracers exhibited very low uptake in nontarget tissues such as muscle (Fig. 3 *A*–*C*).

To demonstrate that $^{64}$Cu-NOTA-Bs-F(ab)$_2$ retained its in vivo specificity toward both EGFR and CD105, we performed blocking studies where mice were administered a large dose (40 mg/kg) of either TRC105 or CET 12 h before injection of $^{64}$Cu-NOTA-Bs-F(ab)$_2$. Peak tumor uptake values of $^{64}$Cu-NOTA-Bs-F(ab)$_2$ dropped significantly to 13.7 ± 2.6%ID/g and 20.3 ± 2.4%ID/g after CD105 and EGFR blocking, respectively ($n$ = 4; Fig. 2 *E* and *F*, Fig. 3 *D* and *E*, and Table S2). Aside from the observed decrease in U87MG uptake values, blocking of CD105 with TRC105 did not alter significantly the overall biodistribution of the radiotracer (Fig. 3*E*). On the other hand, EGFR blocking with CET resulted in decreased liver and kidney uptakes (10.2 ± 2.8%ID/g and 5.7 ± 0.8%ID/g at 3 h p.i., respectively; $n$ = 4; Fig. 3*D*), which corroborates the existence

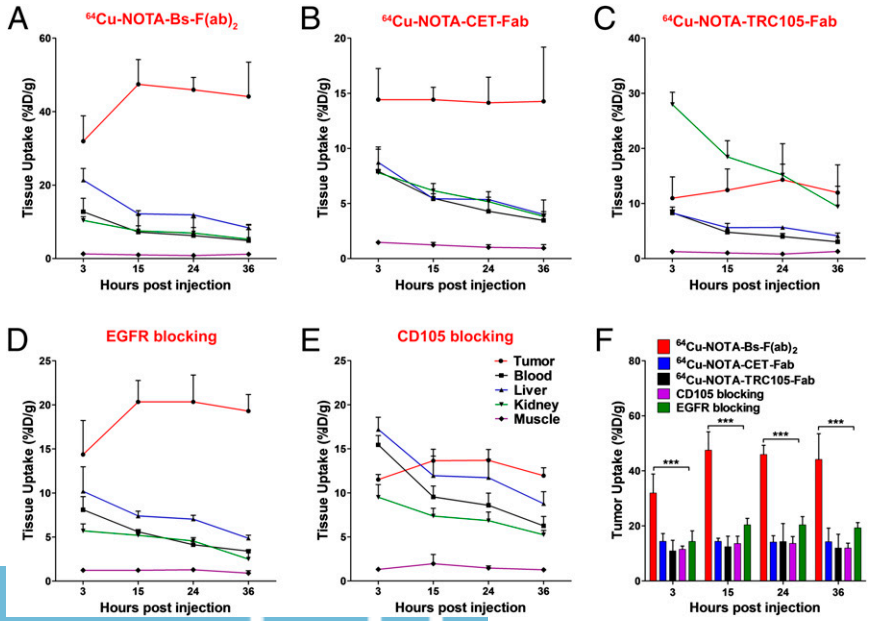


**Fig. 3.** Quantitative ROI analysis of the in vivo PET imaging data. Time-activity curves of U87MG tumor, blood, liver, kidney, and muscle following i.v. administration of $^{64}$Cu-NOTA-Bs-F(ab)$_2$ (*A*), $^{64}$Cu-NOTA-CET-Fab (*B*), $^{64}$Cu-NOTA-TRC105-Fab (*C*), and $^{64}$Cu-NOTA-Bs-F(ab)$_2$ after EGFR (*D*) or CD105 blocking (*E*). (*F*) Comparison of U87MG tumor uptake in all groups based on quantitative analysis of the PET data ($n$ = 4).

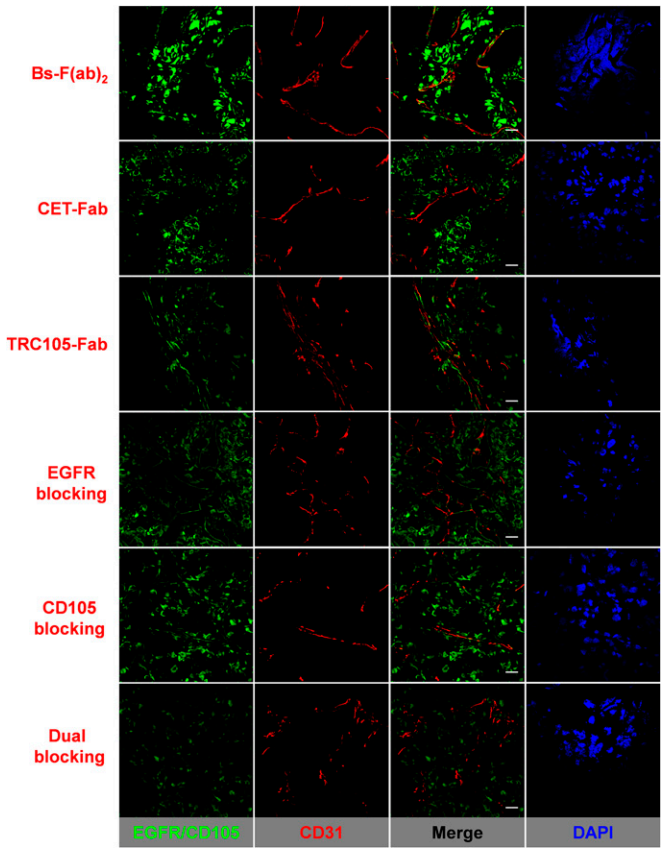


**Fig. 4.** EGFR/CD105 immunofluorescence staining of resected U87MG tumors. FITC-labeled Bs-F(ab)$_2$, CET-Fab, and TRC105-Fab were directly used for EGFR/CD105 staining (green). For blocking experiments, tissue slices were preincubated with 1 mg/mL of either cetuximab, TRC105, or a combination of both full mAbs. Rat anti-mouse CD31 antibody and Cy3-labeled donkey anti-rat IgG were used for CD31 staining (red). DAPI was used to stain cell nuclei. (Scale bar, 20 μm.)

of basal levels of EGFR expression in these organs (25). Overall, only $^{64}$Cu-NOTA-Bs-F(ab)$_2$ uptake in U87MG tumors was significantly ($P < 0.001$ for both blocking groups) affected by CD105/EGFR blocking across all time points (Fig. 3*F*), confirming the dual specificity of $^{64}$Cu-NOTA-Bs-F(ab)$_2$ towards both EGFR and CD105. Taken together, PET data demonstrated that dual targeting using our bispecific tracer offers significant advantages in terms of absolute tumor uptake, target specificity, and off-target uptake over each monospecific Fab fragment.

After the last imaging time point (36 h p.i.), ex vivo biodistribution studies were performed to validate in vivo PET data and obtain a more detailed biodistribution profile of the tracers (Fig. S4 *A* and *B* and Table S3). No statistically significant difference between PET-derived data and the biodistribution data set was observed, certifying that ROI analysis of the PET images accurately described the distribution of the PET tracer in vivo (Fig. S4*D*). The biodistribution profile in normal organs was similar for all three tracers. Also concurrent with PET, an EGFR and CD105 blocking experiment unveiled a drastic decline in U87MG tumor uptake of $^{64}$Cu-NOTA-Bs-F(ab)$_2$, whereas the rest of the analyzed nontarget organs showed marginal changes in tracer accumulation. Owing to such prominent tumor and low background accretion of $^{64}$Cu-NOTA-Bs-F(ab)$_2$, excellent tumor-to-normal ratios were attained at 36 h p.i. of the radiolabeled heterodimer (Table S4). For example, an elevated $^{64}$Cu-NOTA-Bs-F(ab)$_2$ tumor/muscle ratio that was markedly higher (120.2 ± 44.4) than those of $^{64}$Cu-NOTA-CET-Fab (47.6 ± 20.1) and $^{64}$Cu-NOTA-TRC105-Fab (22.5 ± 16.1) was detected at 36 h p.i. (Fig. S4*C*). These results indicated that Bs-F(ab)$_2$ provides high sensitivity and specificity for noninvasive detection of CD105/EGFR-expressing malignancies.

Resected U87MG tumors were stained to correlate high tumor uptake with in situ EGFR and CD105 expression (Fig. 4). Bs-F(ab)$_2$, CET-Fab, and TRC105-Fab were conjugated to FITC and used directly for fluorescent staining of the tumor sections. The allocation of each fragment was consistent with EGFR and CD105 spatial distribution profiles. Concurrent with CD105 expression in proliferating endothelium, TRC105-Fab staining was observed in tumor vasculature, colocalized with CD31 signal. TRC105-Fab signal was also noted in the tumor extravascular space, revealing marked CD105 expression in U87MG cells. On the other hand, CET-Fab was found primarily membrane-bound to EGFR-expressing U87MG cells. Given its EGFR/CD105 ambivalent character, Bs-F(ab)$_2$ staining showed a strong fluorescence signal that distributed within both U87MG tissue and tumor-associated vasculature. EGFR, CD105, and dual blocking resulted in considerably lower Bs-F(ab)$_2$ staining intensity than nonblocked counterparts. More importantly, we were able to confine Bs-F(ab)$_2$ accretion to tumor cells or vasculature based on selectively blocking its binding to either EGFR or CD105, thus reaffirming the CD105/EGFR bispecificity of Bs-F(ab)$_2$.

**Early Tumor Detection with $^{64}$Cu-NOTA-Bs-F(ab)$_2$.** To investigate the potential of our bispecific PET tracer for sensitive detection of small tumor nodules (tumor size, ~20 mm$^3$), $^{64}$Cu-NOTA-Bs-F(ab)$_2$ PET was performed in mice bearing U87MG tumors in the early stages of tumor growth. Sequential coronal images of slices containing small U87MG tumors showed a sharp delineation of small (~3 mm in diameter) tumor contours (Fig. 5*A*). Fig. 5*B* depicts the size range of the fully resected tumors and its corresponding ex vivo PET images at 36 h p.i. Quantitative data obtained from PET ROI analysis uncovered a slower increase in $^{64}$Cu-NOTA-Bs-F(ab)$_2$ uptake for small lesions: from 13.3 ± 8.4%ID/g at 3 h p.i. to 31.4 ± 10.8%ID/g at 36 h p.i. In contrast, $^{64}$Cu-NOTA-Bs-F(ab)$_2$ accumulation in medium-sized tumors was faster and peaked at 15 h p.i. (Fig. 5*C* and Table S1). Ex vivo biodistribution also unveiled notably lower uptake of $^{64}$Cu-NOTA-Bs-F(ab)$_2$ in small U87MG tumors compared with medium-sized tumors (31.4 ± 10.8%ID/g vs. 44.2 ± 9.4%ID/g at 36 h p.i.; $n = 4$). Nonetheless, very high tumor/muscle ratios (76.4 ± 52.3; $n = 3$) were achieved for small tumors at 36 h p.i. (Fig. 5*D* and Table S4). Altogether, these data indicated that $^{64}$Cu-NOTA-Bs-F(ab)$_2$ offers excellent sensitivity for early detection of CD105/EGFR-positive small tumors.

Lastly, we tested the feasibility of Bs-F(ab)$_2$ for image-guided surgery, upon conjugation with the dye ZW800-1. ZW800-Bs-F(ab)$_2$ was i.v. injected into mice bearing small U87MG tumors, and serial near-infrared fluorescence (NIRF) images were recorded at 3, 15, and 24 h p.i. (Fig. 5*E*). NIRF imaging provided accurate tumor localization, which facilitated the complete resection of the tumor. Therefore, we have established the applicability of ZW800-Bs-F(ab)$_2$ for intraoperative image-guided surgical resection of small tumors as well as determination of positive resection margins during surgery.

## Discussion

Despite intense research efforts, current diagnostic and therapeutic strategies have failed to improve significantly the overall survival of patients with GBM, the most common malignant brain tumor, for which 5-y survival remains at a dismal 5% rate (26). EGFR, amplification/mutation of which has been observed in ~57% of GBM patients (27), is recognized as an attractive target for targeted therapy (28). Several EGFR inhibitors have been explored in clinical trials for the treatment of GBM (29); however, poor response and development of resistance have been almost invariably observed. EGFR-mediated up-regulation of several proangiogenic molecules such as vascular endothelial growth factor (VEGF), CD105, $\alpha_v\beta_3$, and Ang-2 (30, 31) by tumor cells has been proposed as one of the mechanism to acquire resistance to EGFR inhibitors (18). Due to this association, combined targeting of EGFR and angiogenic pathways is an appealing strategy to potentially circumvent treatment resistance and improve patient survival. This paradigm has yielded

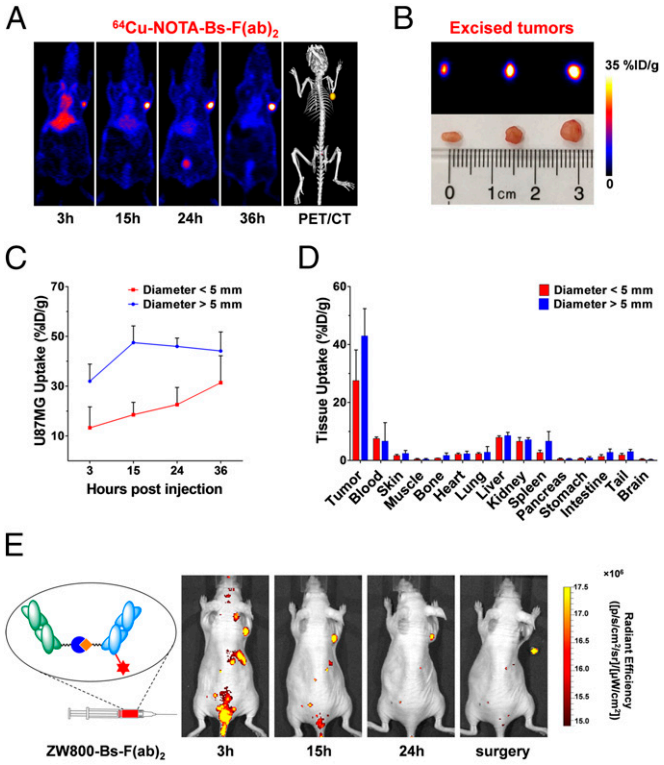


**Fig. 5.** Bs-F(ab)$_2$–based PET imaging and NIRF image-guided surgery of small U87MG tumors. (*A*) Representative PET images of mice bearing a small U87MG tumor at 3, 15, 24, and 36 h following injection of $^{64}$Cu-NOTA-Bs-F(ab)$_2$. (*B*) Ex vivo PET imaging of excised small-diameter (<5 mm) U87MG tumors. Tumors ranged between 0.02 and 0.05 g. (*C*) Comparison of PET-derived time-activity curves for small- versus medium-sized tumors, after i.v. injection of $^{64}$Cu-NOTA-Bs-F(ab)$_2$ in mice bearing U87MG xenografts. (*D*) Ex vivo biodistribution of $^{64}$Cu-NOTA-Bs-F(ab)$_2$ in mice bearing small- versus medium-sized U87MG tumors, at 36 h p.i. ($n = 3$). (*E*) ZW800-Bs-F(ab)$_2$–based serial NIRF imaging enables the accurate tumor localization and image-guided radical excision of small s.c. U87MG lesions.

promising results in several preclinical studies coupling EGFR and VEGFR inhibition for the treatment of GBM (32). Among all EGFR-relevant angiogenic molecules, CD105 captured our attention given that its up-regulation correlates with poor prognosis in a myriad of cancers.

In this study, we sought to investigate the benefits of the simultaneous targeting of EGFR and CD105 in terms of enhanced tumor targeting for early detection of GBM. By chemically linking two Fab fragments from mAb against EGFR and CD105, respectively, we created a heterobifunctional construct possessing excellent in vivo tumor-homing capabilities. Our results from noninvasive PET imaging with $^{64}$Cu-NOTA-Bs-F(ab)$_2$ unveiled a markedly higher tumor uptake of the heterodimer compared with either Fab fragment or whole antibody (23, 33), which indicated that dual EGFR/CD105 targeting provided a synergistic tumor-targeting advantage in U87MG tumors (Figs. 2 and 3). This elevated tumor avidity was corroborated in vitro (Fig. 1 *C* and *D* and Fig. S3). The results of a competitive binding assay revealed notably higher U87MG binding affinity for Bs-F(ab)$_2$ (4.53 ± 0.77 nM) than CET-Fab (393 ± 84 nM) or TRC105-Fab (850 ± 720 nM), supporting the hypothesis of Bs-F(ab)$_2$ ambivalent binding to an increased number of receptors in tumor cells. Due to its higher molecular weight, we noted an enhanced blood circulation of $^{64}$Cu-NOTA-Bs-F(ab)$_2$, which likely played a role in augmenting the observed tumor uptake. More importantly, this targeting advantage did not come at the expense of an increased nonspecific accumulation of the tracer in normal organs, witnessed by a high tumor/muscle ratio of 120.2 ± 44.4 at 36 h following $^{64}$Cu-NOTA-Bs-F(ab)$_2$ administration. Small U87MG tumor nodules (<5 mm) were easily identifiable, owing to high tracer uptake (31.4 ± 10.8%ID/g at 36 h p.i.; $n = 4$) and tumor/muscle ratio (76.4 ± 52.3). In the future, these findings could have significant ramifications for the implementation of combined EGFR and antiangiogenic inhibition therapies, particularly in areas including patient identification, selection, stratification, as well as the monitoring of treatment efficacies.

Heterodimeric immunoconjugates with defined functions can be generated through genetic or biochemical engineering (34, 35). DNA recombination of protein-encoding genes of interest is the most common method to produce bispecific antibodies. Although genetic engineering has been significantly optimized to produce correct fusion proteins, misfolded and inactive products cannot be unequivocally avoided (36). Additionally, common chemical conjugation strategies usually rely on nonspecific cross-linking of amines or sulfhydryl functional groups through heterobifunctional linkers that are highly susceptible to hydrolysis. The employment of these linkers often results in low conjugation yields and the formation of heterogeneous products that complicate downstream separation and purification steps (37). Instead, the use of inverse electron-demand Diels–Alder chemistry, particularly Tz ligation, provides several advantages in terms of simplicity, reaction kinetics, chemoselectivity, lack of a need for catalysts, and high stability of reagents and intermediaries in aqueous media (38, 39). Thus, this bioconjugation strategy is amenable to biological systems and has been successfully applied in vivo for pretargeted radioimmunoimaging (17, 40). The collected body of data demonstrated that TCO/Tz-based bioorthogonal conjugation is a versatile platform that enables rapid, simple, and efficient generation of bispecific constructs that retain or enhance the binding affinity and antigen specificity of their parent monomeric entities. Overall, the success of our production methodology indicates its potential broad applicability for the construction of other heteromeric compounds.

EGFR and CD105 specificity of $^{64}$Cu-NOTA-Bs-F(ab)$_2$ was confirmed, as the preinjection of either parent mAb resulted in a significant abrogation of tumor uptake without affecting tracer biodistribution in the rest of the body. Additionally, immunofluorescence staining of the resected tumors correlated in situ EGFR/CD105 expression with $^{64}$Cu-NOTA-Bs-F(ab)$_2$ tumor accretion. We also observed that CET-Fab and TRC105-Fab primarily targeted cancer cells and cancer-associated vasculature, respectively. Instead, Bs-F(ab)$_2$ was able to localize in both tumor and vascular compartments and provide a targeting advantage over its monomeric counterparts. Taken together, our data demonstrated that $^{64}$Cu-NOTA-Bs-F(ab)$_2$ has desirable properties as a radiotracer for PET imaging of cancer: strong affinity for its target, high specificity, and low off-target accumulation.

In cancer surgery, it is of utmost importance to determine the full extent of the malignancy. This is particularly important in neuro-oncology, where the extent of the surgical resection of brain tumors is a major patient prognosis indicator (41). Radionuclide detection (PET and SPECT) can be used to grossly localize tumor nodules; however, precise delineation of tumor lesions or assessment of tumor surgical margins requires the use of imaging techniques with superior spatial resolution (7). Hence, the fluorophore ZW800-1 was conjugated to Bs-F(ab)$_2$ for NIRF imaging of mice bearing U87MG s.c. xenografts. Consistent with PET imaging results, ZW800-Bs-F(ab)$_2$ displayed prominent tumor accumulation and low/background uptake in nontarget tissues. Owing to the attained high contrasts, we were able to delineate the tumor contours and conduct successful surgical removal (Fig. 5*E*). In a clinical setting, an optical imaging agent based on Bs-F(ab)$_2$ would be of utility to locate the tumor and guide the removal of the tumor foci and surgical margins (42). Similar approaches have shown success in the clinic for the detection/resection of lymph nodes and in patients with ovarian cancer (43, 44).

In an oncology field, where combinatorial diagnostic and therapeutic approaches gain momentum by the day, the clinical implementation of multifunctional pharmaceuticals will certainly occur. The recent FDA approval of Blincyto (blinatumomab, AMGEN), a bispecific antibody for treating B-cell acute lymphoblastic leukemia, has renewed the interest in bispecific antibody technologies (45), and it is likely to spur significant research efforts toward its mainstream implementation. Within that niche, we believe that we have presented a simple molecular engineering platform that is not just restricted to the creation of multimeric antibody constructs but instead has broad applicability to the modification of other biologically active molecules. Our gathered data using two clinically tested antibodies as building blocks for the generation of Bs-F(ab)$_2$ demonstrate that dual-antigen targeting is an effective strategy to enhance tumor targeting, which may ultimately lead to better diagnosis sensitivity and increased therapeutic output. In the future, this paradigm could serve to reevaluate drug candidates that have failed in clinical trials as single agents that otherwise may provide significant therapeutic benefits when combined with the right companion.

## Materials and Methods

All animal studies were conducted under a protocol approved by the University of Wisconsin Institutional Animal Care and Use Committee. Detailed information on reagents, antibody fragment generation, bispecific antibody synthesis and purification, chelator conjugation, $^{64}$Cu labeling, animal models, flow cytometry, competitive binding assay, fluorescent microscopy, PET and NIRF imaging, and ex vivo biodistribution is provided in *SI Materials and Methods*.

**ACKNOWLEDGMENTS.** This work was supported, in part, by the University of Wisconsin–Madison; National Institutes of Health Grants NIBIB/NCI 1R01CA169365, P30CA014520, 5T32GM08349, and T32CA009206; Department of Defense Grants W81XWH-11-1-0644 and W81XWH-11-1-0648; National Science Foundation Grant DGE-1256259; and American Cancer Society Grant 125246-RSG-13-099-01-CCE.

1. Etzioni R, et al. (2003) The case for early detection. *Nat Rev Cancer* 3(4):243–252.
2. James ML, Gambhir SS (2012) A molecular imaging primer: Modalities, imaging agents, and applications. *Physiol Rev* 92(2):897–965.
3. Gambhir SS (2002) Molecular imaging of cancer with positron emission tomography. *Nat Rev Cancer* 2(9):683–693.
4. Larson SM (2004) Positron emission tomography-based molecular imaging in human cancer: Exploring the link between hypoxia and accelerated glucose metabolism. *Clin Cancer Res* 10(7):2203–2204.
5. Abouzied MM, Crawford ES, Nabi HA (2005) 18F-FDG imaging: Pitfalls and artifacts. *J Nucl Med Technol* 33(3):145–155; quiz 162–163.
6. Selzner M, et al. (2004) Does the novel PET/CT imaging modality impact on the treatment of patients with metastatic colorectal cancer of the liver? *Ann Surg* 240(6): 1027–1034; discussion 1035–1036.
7. Hussain T, Nguyen QT (2014) Molecular imaging for cancer diagnosis and surgery. *Adv Drug Deliv Rev* 66:90–100.
8. Knowles SM, Wu AM (2012) Advances in immuno-positron emission tomography: Antibodies for molecular imaging in oncology. *J Clin Oncol* 30(31):3884–3892.
9. Holliger P, Hudson PJ (2005) Engineered antibody fragments and the rise of single domains. *Nat Biotechnol* 23(9):1126–1136.
10. Behr TM, et al. (1995) Reduction of the renal uptake of radiolabeled monoclonal antibody fragments by cationic amino acids and their derivatives. *Cancer Res* 55(17): 3825–3834.
11. Grünberg J, et al. (2005) In vivo evaluation of 177Lu- and 67/64Cu-labeled recombinant fragments of antibody chCE7 for radioimmunotherapy and PET imaging of L1-CAM-positive tumors. *Clin Cancer Res* 11(14):5112–5120.
12. Hanahan D, Weinberg RA (2011) Hallmarks of cancer: The next generation. *Cell* 144(5):646–674.
13. Kontermann RE (2012) Dual targeting strategies with bispecific antibodies. *MAbs* 4(2): 182–197.
14. Luo H, Hong H, Yang SP, Cai W (2014) Design and applications of bispecific heterodimers: Molecular imaging and beyond. *Mol Pharm* 11(6):1750–1761.
15. Scott AM, Wolchok JD, Old LJ (2012) Antibody therapy of cancer. *Nat Rev Cancer* 12(4):278–287.
16. DiGiandomenico A, et al. (2014) A multifunctional bispecific antibody protects against Pseudomonas aeruginosa. *Sci Transl Med* 6(262):262ra155.
17. Rossin R, et al. (2010) In vivo chemistry for pretargeted tumor imaging in live mice. *Angew Chem Int Ed Engl* 49(19):3375–3378.
18. van Cruijsen H, Giaccone G, Hoekman K (2005) Epidermal growth factor receptor and angiogenesis: Opportunities for combined anticancer strategies. *Int J Cancer* 117(6): 883–888.
19. Smith SJ, et al. (2012) CD105 (Endoglin) exerts prognostic effects via its role in the microvascular niche of paediatric high grade glioma. *Acta Neuropathol* 124(1): 99–110.
20. Hong H, Chen F, Zhang Y, Cai W (2014) New radiotracers for imaging of vascular targets in angiogenesis-related diseases. *Adv Drug Deliv Rev* 76:2–20.
21. Hong H, et al. (2012) Multimodality imaging of breast cancer experimental lung metastasis with bioluminescence and a monoclonal antibody dual-labeled with 89Zr and IRDye 800CW. *Mol Pharm* 9(8):2339–2349.
22. Chakravarty R, et al. (2014) Matching the decay half-life with the biological half-life: ImmunoPET imaging with (44)Sc-labeled cetuximab Fab fragment. *Bioconjug Chem* 25(12):2197–2204.
23. Zhang Y, et al. (2013) PET imaging of CD105/endoglin expression with a $^{61/64}$Cu-labeled Fab antibody fragment. *Eur J Nucl Med Mol Imaging* 40(5):759–767.
24. Hong H, et al. (2013) Positron emission tomography imaging of tumor angiogenesis with a (61/64)Cu-labeled F(ab')(2) antibody fragment. *Mol Pharm* 10(2):709–716.
25. Uhlén M, et al. (2015) Proteomics. Tissue-based map of the human proteome. *Science* 347(6220):1260419.
26. Stupp R, et al.; European Organisation for Research and Treatment of Cancer Brain Tumor and Radiotherapy Groups; National Cancer Institute of Canada Clinical Trials Group (2005) Radiotherapy plus concomitant and adjuvant temozolomide for glioblastoma. *N Engl J Med* 352(10):987–996.
27. Brennan CW, et al.; TCGA Research Network (2013) The somatic genomic landscape of glioblastoma. *Cell* 155(2):462–477.
28. Padfield E, Ellis HP, Kurian KM (2015) Current therapeutic advances targeting EGFR and EGFRvIII in glioblastoma. *Front Oncol* 5:5.
29. Carlsson SK, Brothers SP, Wahlestedt C (2014) Emerging treatment strategies for glioblastoma multiforme. *EMBO Mol Med* 6(11):1359–1370.
30. De Luca A, et al. (2008) The role of the EGFR signaling in tumor microenvironment. *J Cell Physiol* 214(3):559–567.
31. Barbu I, Crăiţoiu S, Simionescu CE, Drâgnei AM, Mărgăritescu C (2013) CD105 microvessels density, VEGF, EGFR-1 and c-erbB-2 and their prognostic correlation in different subtypes of cervical adenocarcinoma. *Rom J Morphol Embryol* 54(3): 519–530.
32. Patel M, Vogelbaum MA, Barnett GH, Jalali R, Ahluwalia MS (2012) Molecular targeted therapy in recurrent glioblastoma: Current challenges and future directions. *Expert Opin Investig Drugs* 21(9):1247–1266.
33. Zhang Y, et al. (2011) Positron emission tomography imaging of CD105 expression with a 64Cu-labeled monoclonal antibody: NOTA is superior to DOTA. *PLoS One* 6(12): e28005.
34. Spiess C, et al. (2013) Bispecific antibodies with natural architecture produced by co-culture of bacteria expressing two distinct half-antibodies. *Nat Biotechnol* 31(8): 753–758.
35. Lewis SM, et al. (2014) Generation of bispecific IgG antibodies by structure-based design of an orthogonal Fab interface. *Nat Biotechnol* 32(2):191–198.
36. Witte MD, et al. (2013) Production of unnaturally linked chimeric proteins using a combination of sortase-catalyzed transpeptidation and click chemistry. *Nat Protoc* 8(9):1808–1819.
37. Witte MD, et al. (2012) Preparation of unnatural N-to-N and C-to-C protein fusions. *Proc Natl Acad Sci USA* 109(30):11993–11998.
38. Blackman ML, Royzen M, Fox JM (2008) Tetrazine ligation: Fast bioconjugation based on inverse-electron-demand Diels-Alder reactivity. *J Am Chem Soc* 130(41): 13518–13519.
39. Zeng D, Zeglis BM, Lewis JS, Anderson CJ (2013) The growing impact of bioorthogonal click chemistry on the development of radiopharmaceuticals. *J Nucl Med* 54(6): 829–832.
40. Zeglis BM, et al. (2013) A pretargeted PET imaging strategy based on bioorthogonal Diels-Alder click chemistry. *J Nucl Med* 54(8):1389–1396.
41. Almeida JP, Chaichana KL, Rincon-Torroella J, Quinones-Hinojosa A (2015) The value of extent of resection of glioblastomas: Clinical evidence and current approach. *Curr Neurol Neurosci Rep* 15(2):517.
42. Muselaers CH, et al. (2014) Optical imaging of renal cell carcinoma with anti-carbonic anhydrase IX monoclonal antibody girentuximab. *J Nucl Med* 55(6):1035–1040.
43. van den Berg NS, Valdés-Olmos RA, van der Poel HG, van Leeuwen FW (2013) Sentinel lymph node biopsy for prostate cancer: A hybrid approach. *J Nucl Med* 54(4):493–496.
44. van Dam GM, et al. (2011) Intraoperative tumor-specific fluorescence imaging in ovarian cancer by folate receptor-α targeting: First in-human results. *Nat Med* 17(10): 1315–1319.
45. Sheridan C (2015) Amgen's bispecific antibody puffs across finish line. *Nat Biotechnol* 33(3):219–221.